



Atomic defects engineering on Fe-N₄ sites for boosting oxygen reduction by in-situ ZnO thermal etching strategy

Shengjie Wei ^{a,b,*}, Lei Li ^{c,1}, Ang Li ^{d,1}, Lei Zhang ^{e,1}, Haibo Hu ^e, Dawei Pang ^d, Qinghua Zhang ^f, Hai Xiao ^b, Wenxing Chen ^{g,*}

^a School of Materials Science and Engineering, Nankai University, Tianjin 300350, PR China

^b Department of Chemistry, Tsinghua University, Beijing 100084, PR China

^c Hefei National Research Center for Physical Sciences at the Microscale, University of Science and Technology of China, Hefei, Anhui 230026, PR China

^d Faculty of Materials and Manufacturing, Beijing Key Lab of Microstructure and Properties of Advanced Materials, Beijing University of Technology, Beijing 100124, PR China

^e School of Materials Science and Engineering, Key Laboratory of Structure and Functional Regulation of Hybrid Materials, Ministry of Education, Anhui University, Hefei 230601, PR China

^f Beijing National Laboratory for Condensed Matter Physics, Institute of Physics, Chinese Academy of Sciences, Beijing 100190, PR China

^g Beijing Key Laboratory of Construction Tailorable Advanced Functional Materials and Green Applications, School of Materials Science and Engineering, Beijing Institute of Technology, Beijing 100081, PR China



ARTICLE INFO

Keywords:

Atomic defects engineering
Single-atom sites
Oxygen reduction
In-situ ZnO thermal etching
Zn-air battery

ABSTRACT

Designing atomic defects engineering is significant for boosting the activity of metal catalytic sites. Herein, we constructed Fe-N₄ sites on defective *N*-doped carbon catalyst (Fe-N₄/def-CN) by *in-situ* ZnO thermal etching strategy. Compared with defect-free Fe-N₄/CN, Fe-N₄/def-CN had a half-wave potential ($E_{1/2}$) of 0.920 V vs RHE for alkaline ORR with 50 mV increasing. We directly observed the ZnO *in-situ* disappearance, studied ZnO thermal etching effect on CN substrate and revealed the mechanism of carbon defect formation by *in-situ* environmental transmission electron microscopy (ETEM) and *in-situ* X-ray diffraction (XRD) measurements. Density functional theory (DFT) calculations demonstrated the easier formation of double carbon-atoms defects adjacent to Fe-N₄ sites. The carbon-atoms defects and Zn-atom vacancies synergistically improved the ORR activity of Fe-N₄ sites. This work provides a atomic-level insight to optimize the atomic defects engineering of metal-N₄ sites, such as carbon-atoms defects and metal-atoms vacancies by *in-situ* ZnO thermal etching strategy.

1. Introduction

With increasing global energy consumption, it is significant to design highly efficient and sustainable energy-storage devices, such as fuel cells [1–3] and metal-air batteries [4]. Therefore, it is important to develop highly efficient electro-catalysts for oxygen reduction reaction (ORR) at cathode but with great challenges [5,6]. Currently, Pt-based electro-catalysts exhibited excellent performance for electro-catalysis [7–9], especially as efficient catalysts for ORR [10–13]. However, their scarcity, high-cost and poor stability seriously hindered their large-scale production and further applications. Therefore, it is meaningful to search efficient non-noble metal-based catalysts for ORR to substitute noble Pt-based catalysts [14,15].

Recently, metal isolated single atom sites (ISAS) catalysts have

attracted much attention owing to their utmost atom utilization efficiency, high reactivity, high chemo-selectivity and good stability [16–20]. Among them, metal ISAS catalysts with metal-N₄ sites on *N*-doped carbon (CN) materials served as excellent catalysts for ORR, with the promise to substitute Pt-based electro-catalysts [21–24].

Zeolite Imidazole Framework-8 (ZIF-8), assembled by Zn²⁺ and 2-methylimidazole, has unique advantages as precursor of CN to anchor metal ISAS [25–30]. Zn atoms as metal nodes in ZIF-8 increase atomic distance between metal atoms as guest encapsulated in ZIF-8 and efficiently prevent agglomeration of metal-atoms guest during pyrolysis [31], advantageous to form metal ISAS. Besides, the organic ligand of ZIF-8 is 2-methylimidazole, resulting in high nitrogen content in ZIF-8. After evaporation of Zn element above 900°C, coordination-unsaturated nitrogen atoms as anchoring sites stabilize metal-atoms guests. The high

* Corresponding authors.

E-mail addresses: weishengjie@nankai.edu.cn (S. Wei), wxchen@bit.edu.cn (W. Chen).

¹ S. Wei, L. Li, A. Li and L. Zhang contributed equally to this work.

N content in ZIF-8-derived CN substrates is advantageous to stabilize metal ISAS with high loading. ZIF-8 has abundant micropores with 3.4 Å pores' size and 11.6 Å cavities' size, which can encapsulate metal precursor with suitable diameter as guests in cavities during ZIF-8 crystallization [32], such as metal acetylacetone salts [33–35], metal phthalocyanine salts [24], metal dimer [36] and metal trimer [37]. Therefore, ZIF-8 as an excellent precursor of CN can stabilize a large variety of metal ISAS and metal cluster, such as transition metals [19,22–37], main group metals [21,38] and rare-earth metals [39]. However, it is difficult to fully remove Zn element after pyrolysis of ZIF-8. The residual Zn element will bring disturbance for characterizing and studying catalytic mechanism of metal guests as catalytic active sites.

Optimizing chemical structures of CN substrates, such as morphology, chemical contents and pore size distribution, can regulate chemical environment of metal ISAS and improve their catalytic activities. Recently, introducing carbon-atoms defects around metal ISAS can boost catalytic activity of metal ISAS during electro-catalysis [40,41]. However, we should further develop new synthetic strategy to efficiently introduce carbon-atoms defects around metal ISAS, study different kinds of carbon-atoms defects' probability of formation and formation mechanism, deeply study how carbon-atoms defects influence chemical environment of metal ISAS, modify their electron distribution, optimize interaction between metal ISAS and reaction intermediates for boosting their catalytic performance. Therefore, it is significant to efficiently remove Zn element during pyrolysis of ZIF-8 and skillfully utilize Zn element to introduce carbon-atoms defects around metal-N₄ ISAS, synergistically enhance ORR activity of metal-N₄ ISAS by introduction of carbon-atoms defects and Zn-atoms vacancies on ZIF-derived CN, but with great challenge.

Herein, we synthesized Fe-N₄ ISAS on defective *N*-doped carbon catalyst (Fe-N₄/def-CN) by *in-situ* ZnO thermal etching strategy. Carbon-atoms defects and Zn-atoms vacancies on CN substrates around Fe-N₄ sites synergistically boosted ORR activity of Fe-N₄ sites. Compared with defect-free Fe-N₄ ISAS on CN (Fe-N₄/CN), Fe-N₄/def-CN exhibited enhanced ORR activity, with $E_{1/2}$ of 0.920 V vs RHE in alkaline media, 50 mV higher than Fe-N₄/CN. We directly observed ZnO *in-situ* disappearance and ZnO thermal etching effect on CN substrates, revealing the mechanism of carbon-atoms defects formation by *in-situ* ETEM and *in-situ* XRD measurements. We demonstrated carbon-atoms defects and Zn-atoms vacancies around Fe-N₄ sites could synergistically enhance ORR activity of Fe-N₄ sites by DFT calculation. Fe-N₄ sites on *N*-doped carbon exhibited outstanding reactivity for ORR. It is significant to further boost the reactivity of Fe-N₄ sites for ORR by rationally designing the atomic defect engineering around Fe-N₄ sites, and to study the effect of atomic defect on Fe-N₄ sites during catalysis. In this work, we developed a simple and robust synthetic strategy to introduce carbon-atom defects and Zn-atom vacancies around Fe-N₄ sites by *in-situ* ZnO thermal etching strategy, which improved the reactivity of the Fe-N₄ sites for ORR and shed light on the rational design of atomic defect engineering around the metal-N₄ sites. We directly observed the ZnO thermal etching on carbon by *in-situ* ETEM and *in-situ* XRD measurements, with some inspiration to study the thermal etching effect on substrates.

2. Experimental

2.1. Catalyst preparation

2.1.1. Preparation of ZIF-8

Firstly, 200 ml *N*, *N*-dimethylformamide (DMF) and 50 ml methanol were fixed together and were stirred to obtain homogeneous solution. Then, 10.69 g Zn(NO₃)₂·6H₂O was dissolved in 150 ml above mixed solution by ultrasonic treatment for 10 min. 11.61 g 2-methylimidazole was dissolved in 100 ml above mixed solution by ultrasonic treatment for 10 min. Next, the above Zn(NO₃)₂·6H₂O solution and the above 2-methylimidazole solution were fixed together under room temperature around 25°C, and were stirred violently for several seconds to obtain

homogeneous solution for homogeneous size distribution of ZIF-8. Then, the mixed solution was placed quietly without any stirring for 12 h. Finally, the obtained ZIF-8 powder was collected by centrifugation at 15,000 r.p.m. for 5 min, washed with ethanol for three times and dried at 80°C for 5 h.

2.1.2. Preparation of Fe(acac)₃ molecules loaded on filter papers

1 g Fe(acac)₃ was dissolved in 20 ml ethanol by ultrasonic treatment for 30 min to obtain 50 mg Fe(acac)₃/ml ethanol solution. The Fe(acac)₃/ethanol solution was kept stirring at room temperature. Then, the ordinary filter papers were cut into rectangular shape by 2 cm × 1.5 cm. We immersed the rectangular filter papers into the 50 mg Fe(acac)₃/ml ethanol with stirring for several seconds to absorb the Fe(acac)₃ molecules and removed the redundant Fe(acac)₃ ethanol solution on the surface of filter papers. Then filter papers with Fe(acac)₃ molecules were put into oven at 80°C to evaporate ethanol for preparing the Fe(acac)₃ molecules loaded on filter papers.

2.1.3. Preparation of Fe-N₄/def-CN

The Fe-N₄/def-CN catalyst was synthesized by ZnO thermal etching strategy. As shown in Fig. S1a, eight filter papers (2 cm × 1.5 cm) loading Fe(acac)₃ molecules evenly paved the bottom of ceramic boat. Then, 200 mg ZIF-8 powder homogeneously paved the filter papers with Fe(acac)₃ molecules (Fig. S1b). Next, other eight filter papers (2 cm × 1.5 cm) loading Fe(acac)₃ molecules evenly paved the ZIF-8 powder to form the sandwich-like structure (Fig. S1c). Finally, we placed the ceramic boat loading the precursors in a tube furnace. The sample was heated to 900°C with a heating rate of 5°C/min and we kept the temperature for three hours under flowing argon gas and then the sample was cooled naturally to room temperature. The Fe-N₄/def-CN catalyst was prepared after easy separation between the catalysts and the carbonized filter papers (Fig. S1d). The Fe-CN-400, Fe-CN-500, Fe-CN-600, Fe-CN-700 and Fe-CN-800 catalysts were synthesized by the same synthetic route, except for changing the pyrolysis temperatures at 400°C, 500°C, 600°C, 700°C and 800°C, respectively.

2.1.4. Preparation of def-CN

The def-CN catalyst without Fe loading was also synthesized by ZnO thermal etching strategy. Eight filter papers (2 cm × 1.5 cm) without Fe(acac)₃ molecules loading evenly paved the bottom of ceramic boat. Then, 200 mg ZIF-8 powder homogeneously paved the filter papers. Next, other eight filter papers (2 cm × 1.5 cm) without Fe(acac)₃ molecules loading evenly paved the ZIF-8 powder to form the sandwich-like structure. Finally, we placed the ceramic boat loading the precursors in a tube furnace. The sample was heated to 900°C with a heating rate of 5°C/min and we kept the temperature for three hours under flowing argon gas and then the sample was cooled naturally to room temperature. The def-CN catalyst was prepared after easy separation between the catalyst and the carbonized filter papers.

2.1.5. Preparation of Fe-N₄/CN

The Fe-N₄/CN catalyst without carbon-atoms defects was synthesized by normal pyrolysis of Fe(acac)₃ encapsulated in the pores of ZIF-8 (Fe(acac)₃@ZIF-8). For synthesizing Fe(acac)₃@ZIF-8, 40 ml *N*, *N*-dimethylformamide (DMF) and 10 ml methanol were fixed together and were stirred to obtain homogeneous solution. Then 2138 mg Zn(NO₃)₂·6H₂O and 1270 mg Fe(acac)₃ were dissolved in 30 ml above mixed solution by ultrasonic treatment for 20 min. 2322 mg 2-methylimidazole was dissolved in 20 ml above mixed solution by ultrasonic treatment for 20 min. Next, the above Fe(acac)₃-Zn(NO₃)₂·6H₂O solution and the above 2-methylimidazole solution were fixed together under room temperature around 25°C, and were stirred violently for 24 h. Finally, the obtained Fe(acac)₃@ZIF-8 powder was collected by centrifugation at 15,000 r.p.m. for 5 min, washed with ethanol for six times and dried at 80°C for 5 h. The Fe(acac)₃@ZIF-8 was heated to 900°C with a heating rate of 5°C/min and we kept the temperature for

three hours under flowing argon gas and then the sample was cooled naturally to room temperature.

3. Results and discussion

3.1. Synthesis and characterization of Fe-N₄/def-CN by ZnO thermal etching strategy

We synthesized Fe-N₄/def-CN catalyst by *in-situ* ZnO thermal etching strategy. In Fig. 1a, acetylacetone iron (Fe(acac)₃) loaded on filter papers and ZIF-8 served as precursors of Fe ISAS and CN substrates, respectively. ZIF-8 powder and filter papers with Fe(acac)₃ were assembled into sandwich-like structure and were pyrolyzed together under inert atmosphere at 900°C (Fig. S1). The cellulose from filter papers containing abundant hydroxyl generated H₂O vapor around 340°C, measured by thermogravimetric analysis coupled with fourier-transform infrared spectroscopy and mass spectrometry (TG-FTIR-MS) (Fig. S2). *In-situ* released H₂O vapor reacted with Zn²⁺ ions from ZIF-8 and ZnO nanoparticles (NPs) were *in-situ* formed within ZIF-8 (Fig. 1b and Fig. S3), confirmed by high-resolution high angle annular dark field scanning transmission electron microscopy (HAADF-STEM). Besides, Fe element from Fe(acac)₃ evaporated and was captured by coordination-unsaturated N atoms from ZIF-8 after Zn²⁺ losing. From 400°C to 600°C (Fig. 1b-1d and Fig. S3-S6), ZIF-8 was gradually carbonized and diffraction peaks of ZIF-8 vanished, remaining diffraction peaks of ZnO at 600°C by X-ray diffraction (XRD) measurements (Fig. S7). ZnO NPs' lattice spacing was 0.282 nm by aberration-corrected scanning transmission electron microscopy (AC-STEM), corresponding to ZnO (100) surface (Fig. S8). As pyrolysis temperatures increasing, ZnO NPs reacted with carbon element from substrates, generating CO₂ gas and Zn NPs which evaporated into Zn vapor. ZnO NPs' *in-situ* disappearance was attributed to ZnO thermal etching effect on CN substrates. From 700°C to 900°C, ZnO NPs *in-situ* vanished, confirmed by HAADF-STEM images (Fig. 1e-1 g and Fig. S9-S11) and XRD measurements (Fig. S7). We analyzed structural evolution of Fe-CN catalysts from 600°C to 900°C by extended X-ray absorption fine structure (EXAFS) and AC-STEM measurements. In Fig. 1h, Fe elements existed as Fe ISAS with a prominent Fe-N bond at 1.5 Å on CN substrates without Fe-Fe metallic bond at 2.2 Å from 600°C to 900°C. In Fig. 1i, Zn element existed as Zn ISAS and ZnO with observable Zn-O-Zn bond at 2.8 Å at 600°C. From 700°C to 900°C, Zn ISAS existed with negligible Zn-O-Zn bond attributed to ZnO NPs' *in-situ* disappearance by ZnO thermal etching strategy. AC-STEM measurements revealed ZnO NPs and metal ISAS co-existed in Fe-CN-600 (Fig. S12a-c). The metal ISAS solely existed in Fe-CN-700, Fe-CN-800 and Fe-CN-900 (Fe-N₄/def-CN) (Fig. S12d-f). Fe and Zn contents of Fe-CN catalysts were determined by inductively coupled plasma optical emission spectrometry (ICP-OES) measurements (Table S1). Compared with normal pyrolysis of ZIF-8, ZnO thermal etching strategy could efficiently removed Zn element from CN substrates (Fig. S13). We analyzed the changes of elemental compositions and valence states from Fe-CN-400 to Fe-CN-900 (Fe-N₄/def-CN) by X-ray photoelectron spectroscopy (XPS) measurements in Fig. S14-S20. Intensity of metal-N bond was gradually decreased and Zn-O bond formed as ZnO NPs' *in-situ* formation from 400°C to 600°C (Fig. S20-N and O 1 s spectra). From 600°C to 900°C, contents of Zn-O bond and metal-N bond decreased gradually due to ZnO *in-situ* vanishment and evaporation of Zn element. From 400°C to 900°C, peaks of O 1 s spectra gradually moved to higher binding energy, losing more electrons of O element with transformation from Zn-O bonds to C—O bonds (Fig. S21a). Peaks of Zn 2p spectra moved to lower binding energy with lower valence states due to ZnO *in-situ* disappearance (Fig. S21b). Brunauer-Emmett-Teller (BET) surface areas of Fe-CN catalysts were measured by nitrogen sorption isotherm experiments (Fig. S22 and Fig. S23). During ZnO *in-situ* formation from

400°C to 600°C, BET surface areas decreased sharply. During ZnO *in-situ* disappearance from 600°C to 900°C, BET surface areas increased gradually with formation of abundant mesopores.

We further characterized Fe-N₄/def-CN in Fig. 2. In Fig. 2a and Fig. S11, we confirmed the absence of Fe NPs or ZnO NPs on CN substrates by HAADF-STEM measurements. Energy dispersive X-ray (EDX) spectroscopy elemental mapping results exhibited C, N and Fe elements were homogeneously distributed on CN substrates (Fig. 2b) with 0.88 wt % Fe loading by ICP-OES measurement (Table S1). We directly observed Fe ISAS by AC-STEM measurement and brighter Fe ISAS were marked by white circles in Fig. 2c. We further analyzed components and valence states of Fe element from Fe-N₄/def-CN by ⁵⁷Fe Mössbauer spectroscopy (Fig. 2d and Table S2). The spectrum was composed of three doublets D₁, D₂ and D₃, ascribed to Fe-N_x sites as Fe(III) with high-spin state, Fe (II) with low or medium spin state and Fe(II) with high spin state, respectively [16]. The absence of nulvalent Fe(0) and characteristic sextet component from Fe₂O₃ demonstrated Fe element solely existed as ISAS in Fe-N₄/def-CN. X-ray absorption near-edge structure (XANES) and EXAFS measurements were preformed to characterize Fe-N₄/def-CN. In Fig. 2e, the position of near-edge absorption energy in Fe-N₄/def-CN was between those of Fe foil and α -Fe₂O₃, indicating Fe element from Fe-N₄/def-CN carried partial positive charges. Corresponding Fourier transform (FT) EXAFS curves in R space of Fe-N₄/def-CN, Fe foil and α -Fe₂O₃ were exhibited in Fig. 2f. The spectrum of Fe-N₄/def-CN only showed a prominent peak at 1.5 Å, ascribed to Fe-N bond. The main peak at 2.2 Å from Fe foil was assigned to Fe-Fe bond. Two prominent peaks around 1.5 Å and 3.0 Å from α -Fe₂O₃ were ascribed to Fe-O bond and Fe-O-Fe bond from the second coordination shell, respectively. FT-EXAFS fitting results of Fe-N₄/def-CN were exhibited in Table S3, Fig. S24 and Fig. S25. We performed wavelet transform (WT) of EXAFS oscillation with powerful resolutions in both k and R spaces. In Fig. 2g, intensity maxima in WT contour plot of Fe-N₄/def-CN around 4.0 Å⁻¹ was associated with Fe-N bond, lower than Fe foil around 8 Å⁻¹ associated with Fe-Fe bond (Fig. 2h). Therefore, Fe element was atomically dispersed on Fe-N₄/def-CN by ⁵⁷Fe Mössbauer spectroscopy, FT-EXAFS and WT-EXAFS analysis.

We also synthesized defect-free Fe-N₄/CN catalyst as reference sample by pyrolyzing Fe(acac)₃ encapsulated within ZIF-8 (Fe (acac)₃@ZIF-8) at 900°C. We confirmed atomic dispersion of Fe element in Fe-N₄/CN in Fig. S26-S28. Fe-N₄/CN catalyst had 0.89 wt% Fe loading by ICP-OES, close to Fe-N₄/def-CN with 0.88 wt% Fe loading. Fe-N₄/CN had 9.08 wt% Zn loading, about 14 times that of Fe-N₄/def-CN with 0.65 wt% Zn loading, indicating residual Zn element from ZIF-8-derived CN could be efficiently removed by *in-situ* ZnO thermal etching strategy. XPS spectra of Fe-N₄/CN catalyst were shown in Fig. S29. Compared with Fe-N₄/def-CN, Fe-N₄/CN had lower BET surface area (698 m²/g) and less mesopores (Fig. S30), suggesting ZnO thermal etching strategy facilitated formation of mesopores and increased BET surface area. In Fig. S31, we compared XANES spectra of Fe-N₄/def-CN, Fe-N₄/CN and iron phthalocyanine (FePc). Fe-N₄/def-CN and Fe-N₄/CN had similar XANES spectra to FePc, indicating Fe ISAS existed as Fe-N₄ sites. XANES spectra at Fe L-edge, C K-edge and N K-edge were compared in Fig. S32. We compared the contents of defect between Fe-N₄/def-CN and Fe-N₄/CN by Raman spectra. The Raman spectra were shown in Fig. S33. The disorder peak (D, around 1340 cm⁻¹) [42] was relative to graphite nanocrystalline boundaries and in-plane defects [41]. The graphitic peak (G, around 1580 cm⁻¹) [42] indicated the degree of graphitization [29]. The I_D/I_G value of Fe-N₄/def-CN is 1.11, higher than that of Fe-N₄/CN with I_D/I_G value of 0.97, indicating the higher degree of disorder in Fe-N₄/def-CN by formation of more atomic defects on carbon substrate. We also synthesized Fe-free def-CN by ZnO thermal etching strategy in Fig. S34-S36.

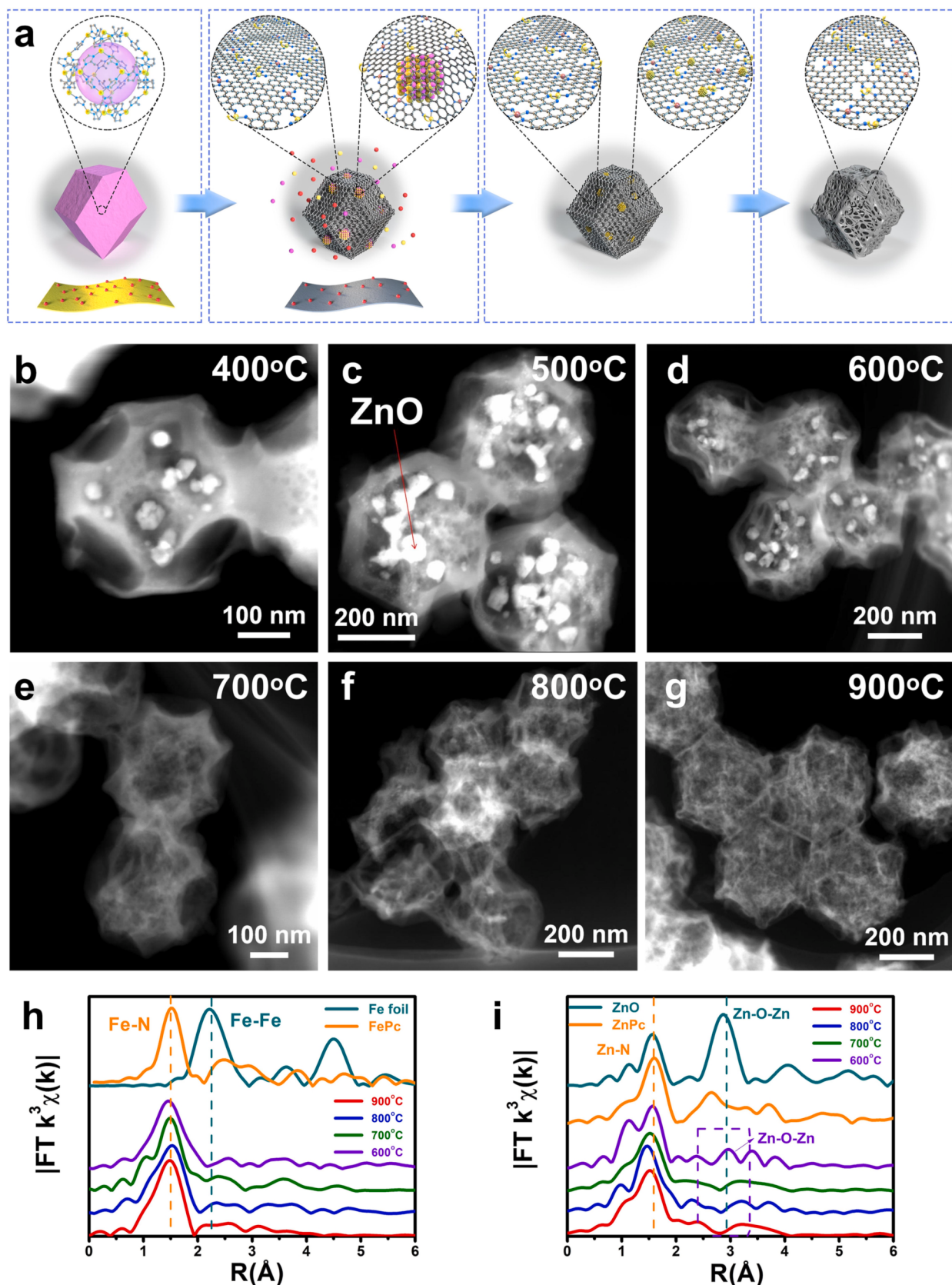


Fig. 1. The ZnO *in-situ* formation and *in-situ* disappearance during the synthesis of Fe-N₄/def-CN by ZnO thermal etching strategy. (a), Schematic illustration of the structural evolution for Fe-N₄/def-CN catalyst. The gray, blue, pink, yellow and red balls represented C, N, O, Zn and Fe atoms, respectively. (b-g), HAADF-STEM images of Fe-CN catalysts by pyrolysis from 400°C to 900°C for 3 h. (h-i), Fourier transforms of k^3 -weighted of Fe and Zn K-edge EXAFS spectra of Fe-CN catalysts. (For interpretation of the references to colour in this figure legend, the reader is referred to the web version of this article.)

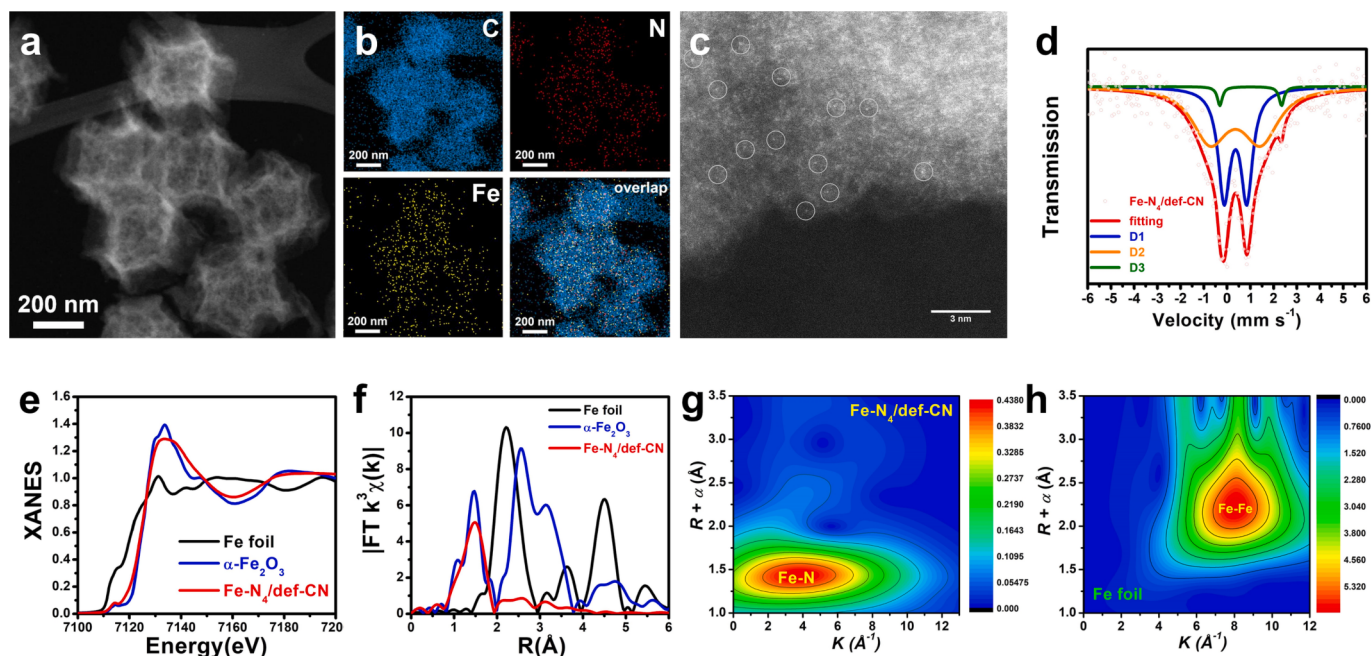


Fig. 2. The characterization of Fe-N₄/def-CN catalyst. (a-b), HAADF-STEM image and corresponding EDX spectroscopy elemental mapping results of Fe-N₄/def-CN. (c), High-resolution AC-STEM image of Fe-N₄/def-CN. (d), The ^{57}Fe Mössbauer spectroscopy and fitting result of Fe-N₄/def-CN. (e-f), The XANES spectra and corresponding FT-EXAFS curves in R space of Fe-N₄/def-CN, Fe foil and α -Fe₂O₃ as reference samples. (g-h), The WT-EXAFS analysis of Fe-N₄/def-CN and Fe foil, respectively.

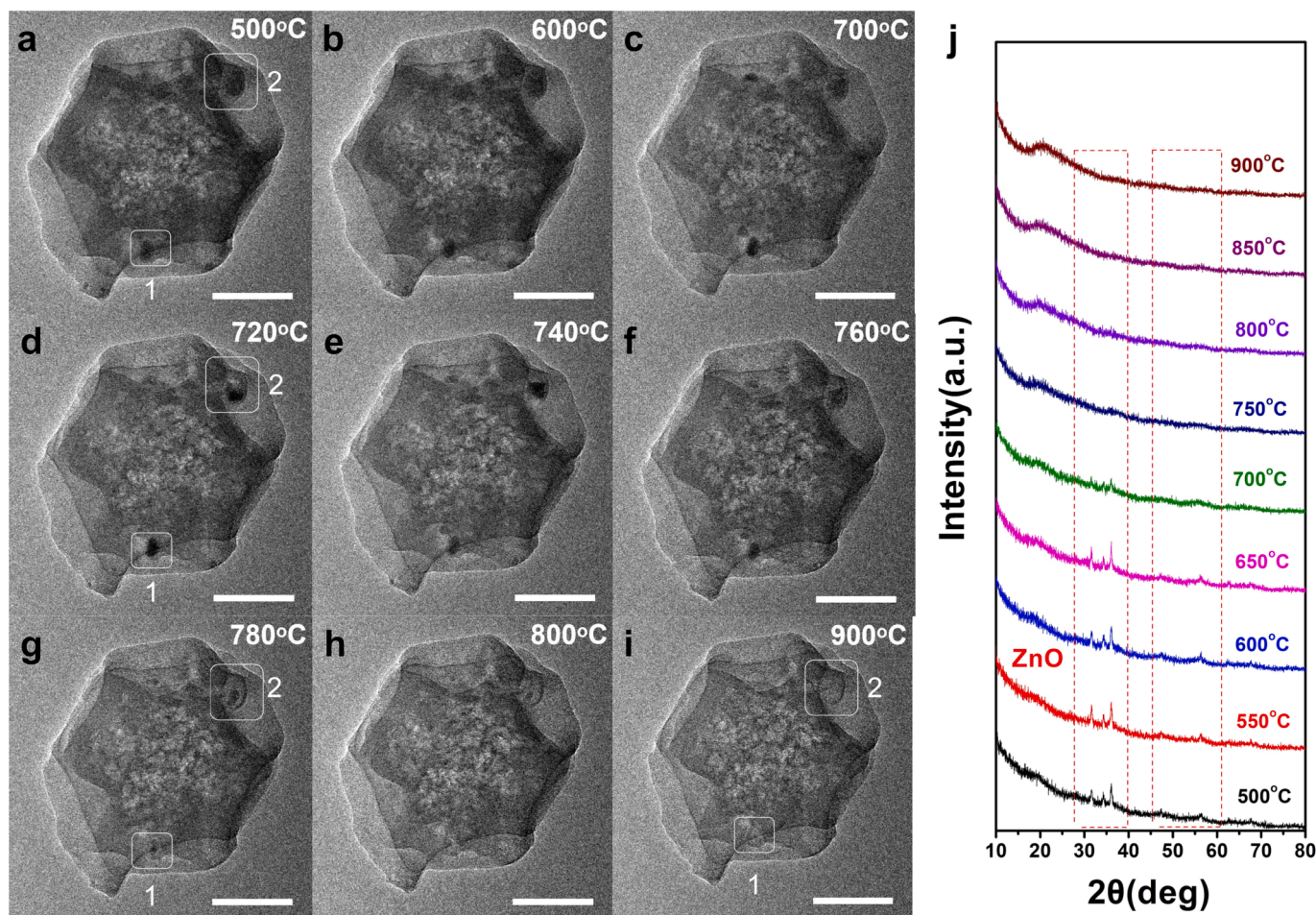


Fig. 3. The *in situ* ETEM and *in situ* XRD measurements of the ZnO thermal etching effect on CN substrate. (a-i), *In-situ* ETEM images during ZnO NPs *in-situ* disappearance by pyrolyzing Fe-CN-600 catalyst from 500°C to 900°C under inert atmosphere. The scale bar was 100 nm. (j), The *in-situ* XRD measurement during ZnO NPs *in-situ* disappearance.

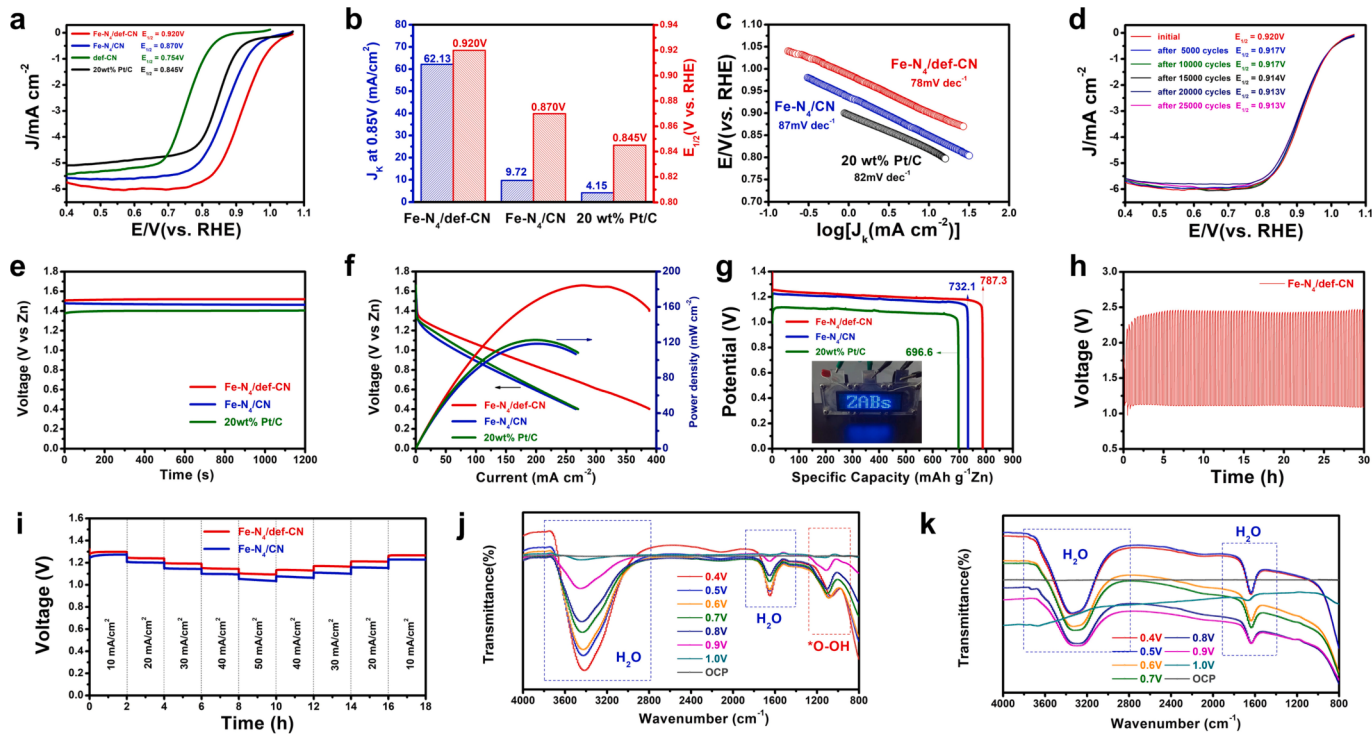


Fig. 4. The alkaline ORR activity and Zn-air battery performance of Fe-N₄/def-CN, Fe-N₄/CN and commercial Pt/C. (a-c), The comparison of LSV curves (a), $E_{1/2}$ (b), J_k at 0.85 V (b) and Tafel slopes (c) between Fe-N₄/def-CN, Fe-N₄/CN and commercial 20 wt% Pt/C. (d), The stability test of Fe-N₄/def-CN during 25,000 cycles. (e-g), For Zn-air battery test, the comparison of open-circuit voltages (e), discharge polarization curves and power density plots (f), and specific discharging capacities (g) between Fe-N₄/def-CN, Fe-N₄/CN and commercial 20 wt% Pt/C. In the inset of (g), the blue light-emitting diode (LED) panel could be easily powered by two tandem Fe-N₄/def-CN based Zn-air batteries. (h), The galvanostatic charge and discharge measurement of Fe-N₄/def-CN. (i), The galvanostatic discharge curves of Fe-N₄/def-CN and Fe-N₄/CN during stability test. (j-k), The *in-situ* ATR-SEIRAS spectroscopy for ORR of Fe-N₄/def-CN catalyst in O₂ and N₂ saturated 0.1 M KOH solution, respectively. (For interpretation of the references to colour in this figure legend, the reader is referred to the web version of this article.)

3.2. Direct observation of ZnO thermal etching effect on carbon substrates

To understand ZnO thermal etching effect on carbon substrates, we directly observed disappearance of ZnO NPs in Fe-CN-600 by *in-situ* ETEM from 500°C to 900°C under Ar atmosphere of 0.08 mbar. In Fig. 3, Fig. S37 and Video S1, ZnO-NP-1 and ZnO-NP-2 circled by white boxes reacted with carbon element from CN substrates at elevated temperatures, with ZnO NPs' size gradually decreasing. Above 840°C, ZnO NPs vanished and mesopores formed by ZnO thermal etching effect on carbon substrates. In Fig. S38, we analyzed variations of size during ZnO NPs' disappearance. The size of ZnO-NP-1 circled by white box-1 decreased from 27.3 nm to 26.1 nm from 500°C to 620°C along the white arrow direction, indicating ZnO thermal etching effect was weak below 620°C. From 620°C to 770°C, the size decreased from 26.1 nm to 21.9 nm, demonstrating ZnO thermal etching accelerated. At 740°C, we measured the spacings of lattice fringe from Zn-based intermediates. In Fig. S39, the spacings of lattice fringe were 0.17 nm, 0.23 nm and 0.25 nm, corresponding to the spacings of Zn nanoparticles' (102), (100) and (002) crystal faces, confirming the transformation from ZnO to Zn NPs by ZnO thermal etching effect on CN substrates. Above 780°C, nanoparticles' size decreased sharply due to extensive evaporation of Zn atoms, from 13.2 nm at 780°C to 6.0 nm at 800°C and 2.8 nm at 840°C. Eventually, ZnO-NP-1 vanished at 860°C. Besides, size of ZnO-NP-2 circled by white box-2 had a similar variation in Fig. 3 and Fig. S40. At 900°C, after ZnO-NP-1 and ZnO-NP-2 vanished, two mesopores formed on carbon substrates, circled by two white boxes in Fig. 3i, with pore size of 25.5 nm and 41.7 nm along two white arrows directions, respectively. *In-situ* disappearance of ZnO-NPs caused shrinkage of CN substrates (Fig. S37). Therefore, ZnO thermal etching experienced the transformation from ZnO NPs into Zn NPs, formation of abundant carbon-atom defects on substrates, evaporation of Zn elements and *in-*

situ disappearance of ZnO NPs.

In-situ XRD measurement also confirmed ZnO NPs *in-situ* disappearance after pyrolyzing Fe-CN-600 at 900°C under Ar atmosphere (Fig. 3j). From 500°C to 750°C, intensity of diffraction peaks from ZnO NPs gradually decreased. Above 750°C, diffraction peaks of ZnO NPs were not observable, indicating ZnO NPs reacted with carbon element from CN substrates and eventually vanished, consistent with *in-situ* ETEM results. Released CO₂ gas was detected during ZnO NPs' *in-situ* disappearance of Fe-CN-600 by TG-FTIR-MS analysis (Fig. S41).

3.3. The catalytic performance for alkaline ORR activity and Zn-air battery

In Fig. 4, alkaline ORR activity of Fe-N₄/def-CN was investigated in O₂-saturated 0.1 M KOH solution. Fig. 4a showed linear sweep voltammetry (LSV) curves of Fe-N₄/def-CN, Fe-N₄/CN, def-CN and commercial 20 wt% Pt/C catalysts. Fe-N₄/def-CN exhibited the best ORR activity with $E_{1/2}$ of 0.920 V, 50 mV, 75 mV and 166 mV higher than those of Fe-N₄/CN, 20 wt% Pt/C and def-CN with $E_{1/2}$ of 0.870 V, 0.845 V and 0.754 V, respectively. Fe-N₄/def-CN also had the highest onset potential (E_{onset}) of 1.055 V. The better ORR activity of Fe-N₄/def-CN than Fe-N₄/CN and def-CN demonstrated Fe-N₄ sites were catalytic sites and defective CN substrates improved ORR activity of Fe-N₄ sites. In Fig. 4b, kinetic current density (J_k) at 0.85 V of Fe-N₄/def-CN was 62.13 mA/cm², about 6.4 times and 15 times those of Fe-N₄/CN (9.72 mA/cm²) and 20 wt% Pt/C (4.15 mA/cm²), respectively. The TOF values and mass activities at 0.85 V of Fe-N₄/def-CN and Fe-N₄/CN were showed in Fig. S42. The mass activity at 0.85 V of Fe-N₄/def-CN was 6.93 A mg⁻¹ Fe, about 6.5 times that of Fe-N₄/CN (1.07 A mg⁻¹ Fe). In Fig. 4c, Fe-N₄/def-CN had a Tafel slope of 78 mV/dec, smaller than Fe-N₄/CN (87 mV/dec) and 20 wt% Pt/C (82 mV/dec). In Table S4, we compared the ORR

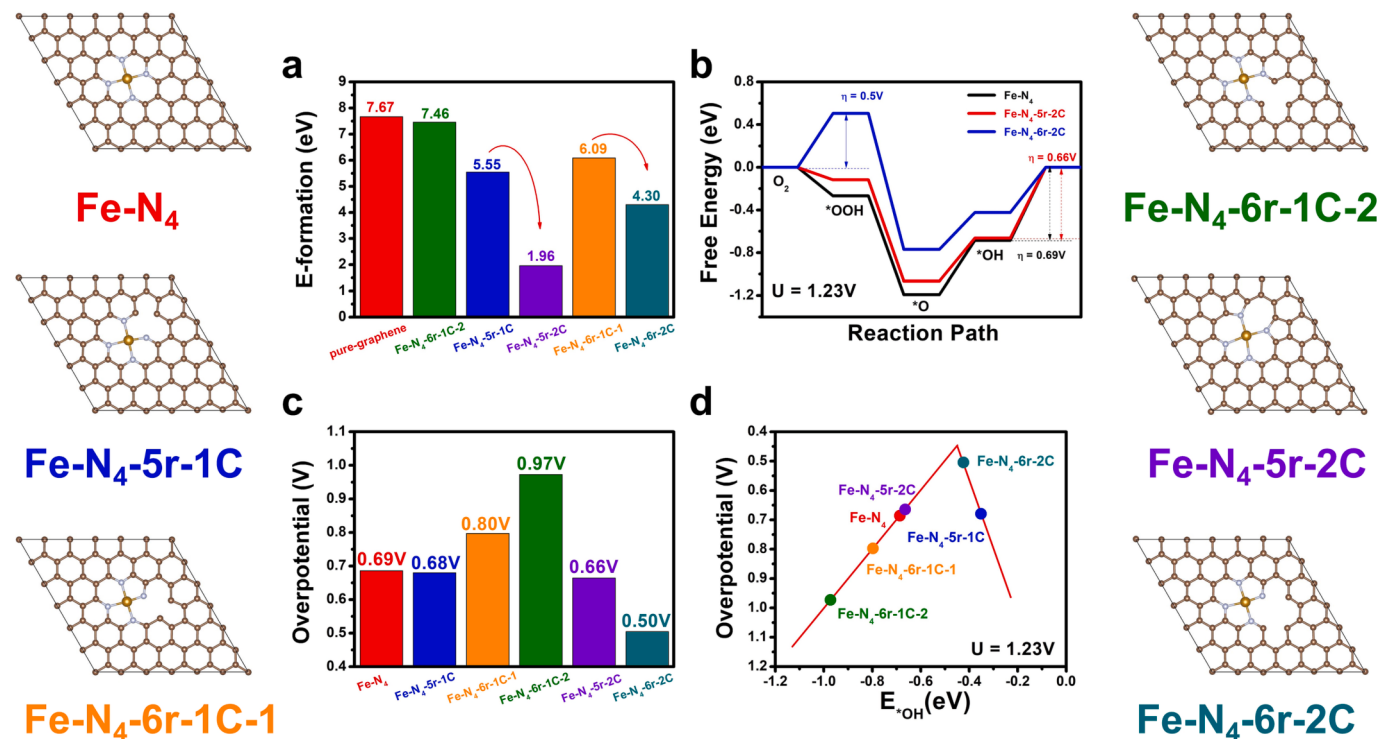


Fig. 5. Density functional theory calculation for ORR on pristine Fe-N₄ and defective Fe-N₄ sites with single or double carbon-atoms defect. (a), The comparison of formation energy between single and double carbon-atoms defect adjacent to Fe-N₄ site. (b), Gibbs free energy diagram for ORR on Fe-N₄ site and Fe-N₄ sites with double carbon-atoms defect. (c), The comparison of overpotentials for ORR between Fe-N₄, single and double carbon-atoms defect adjacent to Fe-N₄ sites. (d), Volcano plot between the adsorption free energies of *OH (E^*_{OH}) and the ORR overpotential. The brown, light blue and dark yellow balls represented C, N and Fe atoms, respectively. (For interpretation of the references to colour in this figure legend, the reader is referred to the web version of this article.)

activity of Fe-N₄/def-CN and other reported non-noble metal-based electro-catalysts. The Fe-N₄/def-CN exhibited outstanding reactivity for ORR among the recently reported non-noble metal-based electro-catalysts, with the $E_{1/2}$ of 0.920 V vs RHE. H_2O_2 yield of Fe-N₄/def-CN was below 3 % from 0.8 V to 0.4 V, measured by rotating ring disk electrode, and electron transfer number was close to 4 (Fig. S43), indicating Fe-N₄/def-CN underwent a four-electron ORR pathway, consistent with the results of Koutecky-Levich (K-L) plots at different rotating rates (Fig. S44). During stability tests, Fe-N₄/def-CN and 20 wt% Pt/C were cycled between 0.7 V and 1.0 V. After 10,000 cycles and 25,000 cycles, $E_{1/2}$ of Fe-N₄/def-CN were 0.917 V and 0.913 V, with $E_{1/2}$ loss of 3 mV and 7 mV, exhibiting excellent ORR stability of Fe-N₄/def-CN (Fig. 4d). After stability test for ORR, we characterized Fe-N₄/def-CN by HAADF-STEM and AC-STEM measurements in Fig. S45. The HAADF-STEM image of Fe-N₄/def-CN after ORR was exhibited in Fig. S45a. No Fe-based nanoparticles were found after ORR. In Fig. S45b, we directly observed the isolated Fe single-atom sites from Fe-N₄/def-CN after ORR by AC-STEM image, indicating the Fe-N₄/def-CN had excellent stability for ORR. ORR stability of 20 wt% Pt/C was poor with $E_{1/2}$ loss of 20 mV after 5000 cycles (Fig. S46). We tested fuel crossover effect of Fe-N₄/def-CN and 20 wt% Pt/C in 0.1 M KOH solution with 1.0 M CH₃OH solution. In Fig. S47, Fe-N₄/def-CN had good methanol tolerance ability with no obvious changes in limited current density and $E_{1/2}$ after adding 1.0 M CH₃OH. While 20 wt% Pt/C had poor ability of methanol tolerance (Fig. S48).

The excellent ORR activity of Fe-N₄/def-CN encouraged us to further explore its potential application in Zn-air battery, with high energy density, low cost and environmental friendliness [43–45]. We assembled Zn-air battery with Fe-N₄/def-CN catalyst as air cathode, Zn foil as anode and 6 M KOH solution as electrolyte. In Fig. 4e, Fe-N₄/def-CN based Zn-air battery exhibited an open-circuit voltage of 1.52 V, higher than Fe-N₄/CN (1.47 V) and 20 wt% Pt/C (1.40 V) based Zn-air battery. In Fig. 4f, Fe-N₄/def-CN based Zn-air battery had the maximum powder

density of 184 mW/cm² at 280 mA/cm², much higher than 20 wt% Pt/C (123 mW/cm² at 202 mA/cm²) and Fe-N₄/CN (119 mW/cm² at 204 mA/cm²) based Zn-air battery. In Fig. 4g, specific capacity of Fe-N₄/def-CN based Zn-air battery was 787.3 mA h/g Zn, higher than 20 wt% Pt/C (696.6 mA h/g Zn) and Fe-N₄/CN (732.1 mA h/g Zn) based Zn-air battery. In Table S5, Fe-N₄/def-CN based Zn-air battery had the maximum power density of 184 mW cm⁻² and specific capacity of 787.3 mA h/g Zn, surpassing most of reported non-noble metal-based electro-catalysts. In Fig. 4h, galvanostatic charge and discharge measurement was performed to study rechargeability and cyclic stability of catalysts. The charge/discharge voltage gap of Fe-N₄/def-CN based Zn-air battery had no obvious changes within 30 h cycling test while those of Fe-N₄/CN and 20 wt% Pt/C based Zn-air battery increased (Fig. S49). The galvanostatic discharge curves of Fe-N₄/def-CN and Fe-N₄/CN based Zn-air battery were exhibited in Fig. 4i. Fe-N₄/def-CN based Zn-air battery showed higher discharge voltages than Fe-N₄/CN from 10 mA/cm² to 50 mA/cm². The discharge voltages of Fe-N₄/def-CN and Fe-N₄/CN based Zn-air battery decreased as current density increasing, then returned to initial potentials as current density decreasing, indicating good stability of the catalysts. We detected oxygenated intermediates adsorbed on Fe-N₄/def-CN for ORR by *in-situ* attenuated total reflection surface-enhanced infrared absorption spectroscopy (ATR-SEIRAS) from 1.0 V to 0.4 V in O₂-saturated 0.1 M KOH solution (Fig. 4j). From 0.9 V to 0.4 V, two negative peaks around 3400 cm⁻¹ and 1650 cm⁻¹ were assigned to adsorbed H₂O [46] and peak around 1100 cm⁻¹ was attributed to *OOH intermediate [47], indicating Fe-N₄/def-CN underwent associative mechanism rather than dissociative mechanism during ORR [29]. In Fig. 4k, *OOH intermediate vanished in N₂-saturated 0.1 M KOH solution, suggesting *OOH intermediate derived from reduction of O₂ in solution.

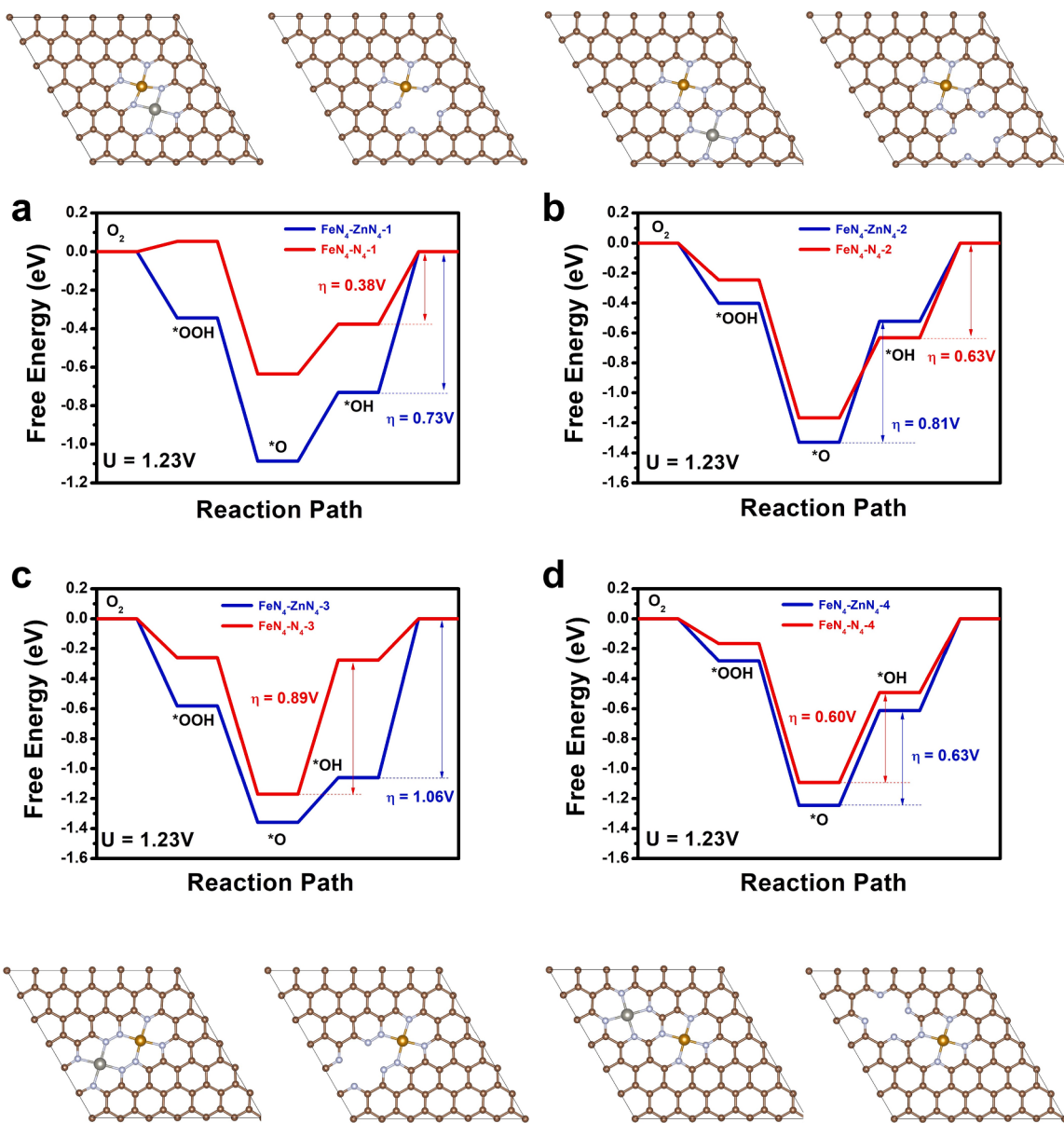


Fig. 6. Density functional theory calculation for ORR on $\text{FeN}_4\text{-ZnN}_4$ sites and $\text{FeN}_4\text{-N}_4$ sites with adjacent Zn-atom vacancy. (a-d), Gibbs free energy diagrams for ORR and corresponding structures of different $\text{FeN}_4\text{-ZnN}_4$ sites and $\text{FeN}_4\text{-N}_4$ sites. The brown, light blue, gray and dark yellow balls represented C, N, Zn and Fe atoms, respectively. (For interpretation of the references to colour in this figure legend, the reader is referred to the web version of this article.)

3.4. Density functional theory calculation for ORR

Density functional theory (DFT) calculation was performed to compare the possibility of formation for different carbon-atoms defects around Fe-N_4 sites on N -doped graphene and study the influence of different carbon-atoms defects on ORR activity of Fe-N_4 sites. We constructed pristine Fe-N_4 site on N -doped graphene and 5 possible models of defective Fe-N_4 sites with different carbon-atoms defects (Fig. 5). We calculated formation energies of above defective Fe-N_4 sites to compare their possibility of formation (Fig. 5a). The formation energy of Fe-N_4 -site-free graphene with one carbon-atom defect was 7.67 eV. By comparison, it was more easier to form single carbon-atom defect around Fe-N_4 site on N -doped graphene, such as $\text{Fe-N}_4\text{-5r-1C}$ (5.55 eV), $\text{Fe-N}_4\text{-6r-1C-1}$ (6.09 eV) and $\text{Fe-N}_4\text{-6r-1C-2}$ (7.46 eV). Compared with $\text{Fe-N}_4\text{-6r-1C-2}$, formation energies of $\text{Fe-N}_4\text{-5r-1C}$ and $\text{Fe-N}_4\text{-6r-1C-1}$ were lower, indicating the easier formation of single carbon-atom defect adjacent to Fe-N_4 site. Compared with single carbon-atom defect, formation energies of double carbon-atoms defects around Fe-N_4 site were much

lower, such as $\text{Fe-N}_4\text{-5r-2C}$ (1.96 eV) and $\text{Fe-N}_4\text{-6r-2C}$ (4.30 eV), demonstrating easier formation of double carbon-atoms defects around Fe-N_4 site than single carbon-atom defect.

We calculated Gibbs free energy changes on pristine Fe-N_4 site and different defective Fe-N_4 sites during $4e^-$ ORR at 1.23 V. The structures of adsorbed $^*\text{OOH}$, $^*\text{O}$ and $^*\text{OH}$ on different Fe-N_4 sites were exhibited in Fig. S50–S55. In Fig. 5b, potential-determining step (PDS) for ORR of pristine Fe-N_4 site without carbon-atoms defect was reduction of $^*\text{OH}$, with overpotential (η_{ORR}) of 0.69 V. For defective Fe-N_4 sites with double carbon-atoms defects, PDS for ORR on $\text{Fe-N}_4\text{-5r-2C}$ was reduction of $^*\text{OH}$, with η_{ORR} of 0.66 V. For $\text{Fe-N}_4\text{-6r-2C}$, PDS for ORR was reduction of $^*\text{O}_2$, with η_{ORR} of 0.50 V. Compared with pristine Fe-N_4 site, defective Fe-N_4 sites with double carbon-atoms defects significantly reduced η_{ORR} and boosted ORR activity. The ORR pathway on Fe-N_4 sites with single carbon-atom defect was exhibited in Fig. S56. Considering formation energies, it was much easier to form double carbon-atoms defects around Fe-N_4 site than single carbon-atom defect (Fig. 5a) and defective Fe-N_4 sites with double carbon-atoms defects

efficiently enhanced ORR activity (Fig. 5b and Fig. 5c), consistent with experimental results that carbon-defect-rich Fe-N₄/def-CN exhibited much better ORR activity than carbon-defect-free Fe-N₄/CN.

For ORR, adsorption energy of *OH (E_{*OH}) on catalytic sites is related to ORR activity [48,49]. Therefore, we studied relationship between η_{ORR} and E_{*OH} on pristine Fe-N₄ site and different Fe-N₄ sites with carbon-atoms defects. In Fig. 5d, it exhibited a volcano relationship between η_{ORR} and E_{*OH}, in which Fe-N₄-6r-2C site was closest to the peak of volcanic curve with the minimum η_{ORR} of 0.5 V, indicating moderate E_{*OH} was advantageous to boost ORR activity. We analyzed the interaction between adsorbed *OH and different Fe-N₄ sites by charge density difference in Fig. S57 and Fig. S58.

Except for carbon-atoms defects effect on ORR, it could effectively decreased Zn content of Fe-N₄/def-CN catalyst by ZnO thermal etching strategy. In Table S1, Fe-N₄/def-CN had 0.65 wt% Zn loading, much lower than Fe-N₄/CN with 9.08 wt% Zn loading. The coordination-unsaturated N₄ sites without Zn atom were introduced into N-doped carbon around Fe-N₄ sites after removal of Zn atoms by ZnO thermal etching strategy. We also studied the effect of coordination-unsaturated N₄ sites without Zn atom around Fe-N₄ sites for ORR, compared with the effect of Zn-N₄ sites around Fe-N₄ sites for ORR by DFT calculation.

In Fig. 6, we constructed four possible models containing Zn-N₄ sites adjacent to Fe-N₄ sites. Then we removed Zn atom from Zn-N₄ site to construct coordination-unsaturated N₄ sites adjacent to Fe-N₄ site. In Fig. 6a, PDSs for ORR on FeN₄-ZnN₄-1 and FeN₄-N₄-1 sites were reduction of *OH, η_{ORR} of FeN₄-N₄-1 site was much lower than FeN₄-ZnN₄-1 site (0.38 V v.s. 0.73 V). In Fig. 6b, PDSs for ORR on FeN₄-ZnN₄-2 and FeN₄-N₄-2 sites were reduction of *O and *OH, with η_{ORR} of 0.81 V and 0.63 V, respectively. In Fig. 6c, PDSs for FeN₄-ZnN₄-3 and FeN₄-N₄-3 sites were reduction of *OH and *O, with η_{ORR} of 1.06 V and 0.89 V, respectively. In Fig. 6d, PDSs for FeN₄-ZnN₄-4 and FeN₄-N₄-4 sites were reduction of *O, with η_{ORR} of 0.63 V and 0.60 V, respectively. Therefore, coordination-unsaturated N₄ sites after removal of Zn atom adjacent to Fe-N₄ sites could effectively boost ORR activity with lower η_{ORR}. The structures of adsorbed *OOH, *O and *OH on different catalytic sites were exhibited in Fig. S59–S66. We also compared formation energies of above FeN₄-ZnN₄ and FeN₄-N₄ sites in Fig. S67. DFT calculation demonstrated carbon-atoms defects and Zn-atoms vacancies around Fe-N₄ sites synergistically boosted ORR activity by ZnO thermal etching strategy.

4. Conclusions

In summary, we synthesized defective Fe-N₄/def-CN by *in-situ* ZnO thermal etching strategy. Compared with defects-free Fe-N₄/CN, Fe-N₄/def-CN exhibited enhanced ORR activity, with E_{1/2} of 0.92 V and excellent stability for alkaline ORR. We directly observed ZnO *in-situ* disappearance by *in-situ* ETEM and *in-situ* XRD, revealing ZnO thermal etching effect on carbon substrates. DFT calculation demonstrated the adjacent carbon-atoms defects and Zn-atom vacancies synergistically boosted ORR activity of Fe-N₄ sites. This work will provide some insights for rationally designing atomic defects engineering on metal catalytic sites and optimizing their catalytic activity.

Declaration of Competing Interest

The authors declare that they have no known competing financial interests or personal relationships that could have appeared to influence the work reported in this paper.

Data availability

The data that has been used is confidential.

Acknowledgements

This work was supported by the National Postdoctoral Program for Innovative Talents of China (No. BX20220159) and the National Natural Science Foundation of China (21890383). We thank the 1W1B station for XAFS measurements in Beijing Synchrotron Radiation Facility (BSRF), China. We thank the BL11U beamline and Beamlines MCD-A and MCD-B (Soochow Beamline for Energy Materials) at National Synchrotron Radiation Laboratory (NSRL), China for the XANES spectroscopy measurements. We acknowledge the Center for Advanced Mössbauer Spectroscopy, Mössbauer Effect Data Center, Dalian Institute of Chemical Physics, CAS, for providing the Mössbauer measurement and analysis. The numerical calculations in this paper have been done on the supercomputing system in the Supercomputing Center of the University of Science and Technology of China.

Appendix A. Supplementary data

Supplementary data to this article can be found online at <https://doi.org/10.1016/j.cej.2023.142820>.

References

- [1] X. Tian, X. Zhao, Y.-Q. Su, L. Wang, H. Wang, D. Dang, B. Chi, H. Liu, E.J. M. Hensen, X.W. Lou, B.Y. Xia, Engineering bunched Pt-Ni alloy nanocages for efficient oxygen reduction in practical fuel cells, *Science* 366 (2019) 850–856.
- [2] X. Wan, Q. Liu, J. Liu, S. Liu, X. Liu, L. Zheng, J. Shang, R. Yu, J. Shui, Iron atom-cluster interactions increase activity and improve durability in Fe-N-C fuel cells, *Nat. Commun.* 13 (2022) 2963.
- [3] Z.-P. Wu, D.T. Caracciolo, Y. Masmadeh, J. Wen, Z. Kong, S. Shan, J.A. Vargas, S. Yan, E. Hopkins, K. Park, A. Sharma, Y. Ren, V. Petkov, L. Wang, C.-J. Zhong, Alloying-reallying enabled high durability for Pt-Pd-3d-transition metal nanoparticle fuel cell catalysts, *Nat. Commun.* 12 (2021) 859.
- [4] Q. Wang, Q. Feng, Y. Lei, S. Tang, L. Xu, Y. Xiong, G. Fang, Y. Wang, P. Yang, J. Liu, W. Liu, X. Xiong, Quasi-solid-state Zn-air batteries with an atomically dispersed cobalt electrocatalyst and organohydrogel electrolyte, *Nat. Commun.* 13 (2022) 3689.
- [5] X. Tian, X.F. Lu, B.Y. Xia, X.W. Lou, Advanced Electrocatalysts for the Oxygen Reduction Reaction in Energy Conversion Technologies, *Joule* 4 (2020) 45–68.
- [6] J. Wang, H.L. Xin, J. Zhu, S. Liu, Z. Wu, D. Wang, 3D hollow structured Co₂FeO₄/MWCNT as an efficient non-precious metal electrocatalyst for oxygen reduction reaction, *J. Mater. Chem. A* 3 (2015) 1601–1608.
- [7] Z. Wu, P. Yang, Q. Li, W. Xiao, Z. Li, G. Xu, F. Liu, B. Jia, T. Ma, S. Feng, L. Wang, Microwave Synthesis of Pt Clusters on Black TiO₂ with Abundant Oxygen Vacancies for Efficient Acidic Electrocatalytic Hydrogen Evolution, *Angew. Chem. Int. Ed.* (2023) e202300406.
- [8] W. Yu, Z. Chen, Y. Fu, W. Xiao, B. Dong, Y. Chai, Z. Wu, L. Wang, Superb All-pH Hydrogen Evolution Performances Powered by Ultralow Pt-Decorated Hierarchical Ni-Mo Porous Microcolumns, *Adv. Funct. Mater.* 33 (2023) 2210855.
- [9] Z. Wu, Y. Zhao, W. Xiao, Y. Fu, B. Jia, T. Ma, L. Wang, Metallic-Bonded Pt-Co for Atomically Dispersed Pt in the Co₄N Matrix as an Efficient Electrocatalyst for Hydrogen Generation, *ACS Nano* 16 (2022) 18038–18047.
- [10] F. Xiao, Q. Wang, G.-L. Xu, X. Qin, I. Hwang, C.-J. Sun, M. Liu, W. Hua, H. Wu, S. Zhu, J.-C. Li, J.-G. Wang, Y. Zhu, D. Wu, Z. Wei, M. Gu, K. Amine, M. Shao, Atomically dispersed Pt and Fe sites and Pt-Fe nanoparticles for durable proton exchange membrane fuel cells, *Nat. Catal.* 5 (2022) 503–512.
- [11] R. Gao, J. Wang, Z.-F. Huang, R. Zhang, W. Wang, L. Pan, J. Zhang, W. Zhu, X. Zhang, C. Shi, J. Lim, J.-J. Zou, Pt/Fe₂O₃ with Pt-Fe pair sites as a catalyst for oxygen reduction with ultralow Pt loading, *Nat. Energy* 6 (2021) 614–623.
- [12] G.W. Sievers, A.W. Jensen, J. Quinson, A. Zana, F. Bizzotto, M. Oezaslan, A. Dworzak, J.J.K. Kirkengaard, T.E.L. Smitshuysen, S. Kadkhodazadeh, M. Juelskolt, K.M.Ø. Jensen, K. Anklam, H. Wan, J. Schäfer, K. Cépe, M. Escudero-Escriciano, J. Rossmieis, A. Quade, V. Brüser, M. Arenz, Self-supported Pt-CoO networks combining high specific activity with high surface area for oxygen reduction, *Nat. Mater.* 20 (2021) 208–213.
- [13] Z. Zhao, Z. Liu, A. Zhang, X. Yan, W. Xue, B. Peng, H.L. Xin, X. Pan, X. Duan, Y. Huang, Graphene-nanopocket-encaged PtCo nanocatalysts for highly durable fuel cell operation under demanding ultralow-Pt-loading conditions, *Nat. Nanotechnol.* 17 (2022) 968–975.
- [14] Y. Zhou, X. Tao, G. Chen, R. Lu, D. Wang, M.-X. Chen, E. Jin, J. Yang, H.-W. Liang, Y. Zhao, X. Feng, A. Narita, K. Müllen, Multilayer stabilization for fabricating high-loading single-atom catalysts, *Nat. Commun.* 11 (2020) 5892.
- [15] J. Gao, H. Yang, X. Huang, S.-F. Hung, W. Cai, C. Jia, S. Miao, H.M. Chen, X. Yang, Y. Huang, T. Zhang, B. Liu, Enabling Direct H₂O₂ Production in Acidic Media through Rational Design of Transition Metal Single Atom Catalyst, *Chem* 6 (2020) 658–674.
- [16] A. Mehmood, M. Gong, F. Jaouen, A. Roy, A. Zitolo, A. Khan, M.-T. Sougrati, M. Primb, A.M. Bonastre, D. Fongalland, G. Drazic, P. Strasser, A. Kucernak, High

- loading of single atomic iron sites in Fe-NC oxygen reduction catalysts for proton exchange membrane fuel cells, *Nat. Catal.* 5 (2022) 311–323.
- [17] Z. Li, R. Wu, S. Xiao, Y. Yang, L. Lai, J.S. Chen, Y. Chen, Axial chlorine coordinated iron–nitrogen–carbon single-atom catalysts for efficient electrochemical CO₂ reduction, *Chem. Eng. J.* 430 (2022), 132882.
- [18] Y. Wang, K. Liu, J. Li, X. Yang, J. Hu, T.-S. Chan, X. Qiu, W. Li, M. Liu, CoN₄ active sites in locally distorted carbon structure for efficient oxygen reduction reaction via regulating coordination environment, *Chem. Eng. J.* 429 (2022), 132119.
- [19] S. Wei, A. Li, J.-C. Liu, Z. Li, W. Chen, Y. Gong, Q. Zhang, W.-C. Cheong, Y. Wang, L. Zheng, H. Xiao, C. Chen, D. Wang, Q. Peng, L. Gu, X. Han, J. Li, Y. Li, Direct observation of noble metal nanoparticles transforming to thermally stable single atoms, *Nat. Nanotech.* 13 (2018) 856–861.
- [20] Z.-X. Wei, Y.-T. Zhu, J.-Y. Liu, Z.-C. Zhang, W.-P. Hu, H. Xu, Y.-Z. Feng, J.-M. Ma, Recent advance in single-atom catalysis, *Rare Met.* 40 (2021) 767.
- [21] T. Wang, X. Cao, H. Qin, L. Shang, S. Zheng, F. Fang, L. Jiao, P-Block Atomically Dispersed Antimony Catalyst for Highly Efficient Oxygen Reduction Reaction, *Angew. Chem. Int. Ed.* 60 (2021) 21237.
- [22] J. Qin, H. Liu, P. Zou, R. Zhang, C. Wang, H.L. Xin, Altering Ligand Fields in Single-Atom Sites through Second-Shell Anion Modulation Boosts the Oxygen Reduction Reaction, *J. Am. Chem. Soc.* 144 (2022) 2197–2207.
- [23] X. Li, C.-S. Cao, S.-F. Hung, Y.-R. Lu, W. Cai, A.I. Rykov, S. Miao, S. Xi, H. Yang, Z. Hu, J. Wang, J. Zhao, E.E. Alp, W. Xu, T.-S. Chan, H. Chen, Q. Xiong, H. Xiao, Y. Huang, J. Li, T. Zhang, B. Liu, Identification of the Electronic and Structural Dynamics of Catalytic Centers in Single-Fe-Atom Material, *Chem* 6 (2020) 3440–3454.
- [24] M. Liu, N. Li, S. Cao, X. Wang, X. Lu, L. Kong, Y. Xu, X.-H. Bu, A “Pre-Constrained Metal Twins” Strategy to Prepare Efficient Dual-Metal-Atom Catalysts for Cooperative Oxygen Electrocatalysis, *Adv. Mater.* 34 (2022) 2107421.
- [25] Y. Chen, S. Ji, S. Zhao, W. Chen, J. Dong, W.-C. Cheong, R. Shen, X. Wen, L. Zheng, A.I. Rykov, S. Cai, H. Tang, Z. Zhuang, C. Chen, Q. Peng, D. Wang, Y. Li, Enhanced oxygen reduction with single-atomic-site iron catalysts for a zinc-air battery and hydrogen-air fuel cell, *Nat. Commun.* 9 (2018) 5422.
- [26] H. Shang, X. Zhou, J. Dong, A. Li, X. Zhao, Q. Liu, Y. Lin, J. Pei, Z. Li, Z. Jiang, D. Zhou, L. Zheng, Y. Wang, J. Zhou, Z. Yang, R. Cao, R. Sarangi, T. Sun, X. Yang, X. Zheng, W. Yan, Z. Zhuang, J. Li, W. Chen, D. Wang, J. Zhang, Y. Li, Engineering unsymmetrically coordinated Cu-Si₃N₄ single atom sites with enhanced oxygen reduction activity, *Nat. Commun.* 11 (2020) 3049.
- [27] M. Chang, Z. Hou, M. Wang, C. Yang, R. Wang, F. Li, D. Liu, T. Peng, C. Li, J. Lin, Single-Atom Pd Nanozyme for Ferroptosis-Boosted Mild-Temperature Photothermal Therapy, *Angew. Chem. Int. Ed.* 60 (2021) 12971.
- [28] C. Liu, Y. Wu, K. Sun, J. Fang, A. Huang, Y. Pan, W.-C. Cheong, Z. Zhuang, Z. Zhuang, Q. Yuan, H.L. Xin, C. Zhang, J. Zhang, H. Xiao, C. Chen, Y. Li, Constructing FeN₄/graphitic nitrogen atomic interface for high-efficiency electrochemical CO₂ reduction over a broad potential window, *Chem* 7 (2021) 1297–1307.
- [29] Y. Chen, R. Gao, S. Ji, H. Li, K. Tang, P. Jiang, H. Hu, Z. Zhang, H. Hao, Q. Qu, X. Liang, W. Chen, J. Dong, D. Wang, Y. Li, Atomic-level modulation of electronic density of metal–organic frameworks-derived Co single-atom sites to enhance oxygen reduction performance, *Angew. Chem. Int. Ed.* 60 (2021) 3212.
- [30] Q. Liu, Y. Li, L. Zheng, J. Shang, X. Liu, R. Yu, J. Shui, Sequential Synthesis and Active-Site Coordination Principle of Precious Metal Single-Atom Catalysts for Oxygen Reduction Reaction and PEM Fuel Cells, *Adv. Energy Mater.* 10 (2020) 2000689.
- [31] P. Yin, T. Yao, Y. Wu, L. Zheng, Y. Lin, W. Liu, H. Ju, J. Zhu, X. Hong, Z. Deng, G. Zhou, S. Wei, Y. Li, Single Cobalt Atoms with Precise N-Coordination as Superior Oxygen Reduction Reaction Catalysts, *Angew. Chem. Int. Ed.* 55 (2016) 10800.
- [32] Z. Li, Y. Chen, S. Ji, Y. Tang, W. Chen, A. Li, J. Zhao, Y. Xiong, Y. Wu, Y. Gong, T. Yao, W. Liu, L. Zheng, J. Dong, Y. Wang, Z. Zhuang, W. Xing, C.-T. He, C. Peng, W.-C. Cheong, Q. Li, M. Zhang, Z. Chen, N. Fu, X. Gao, W. Zhu, J. Wan, J. Zhang, L. Gu, S. Wei, P. Hu, J. Luo, J. Li, C. Chen, Q. Peng, X. Duan, Y. Huang, X.-M. Chen, D. Wang, Y. Li, Iridium single-atom catalyst on nitrogen-doped carbon for formic acid oxidation synthesized using a general host-guest strategy, *Nat. Chem.* 12 (2020) 764–772.
- [33] Y. Chen, S. Ji, Y. Wang, J. Dong, W. Chen, Z. Li, R. Shen, L. Zheng, Z. Zhuang, D. Wang, Y. Li, Isolated Single Iron Atoms Anchored on N-Doped Porous Carbon as an Efficient Electrocatalyst for the Oxygen Reduction Reaction, *Angew. Chem. Int. Ed.* 56 (2017) 6937.
- [34] Y. Wang, G. Jia, X. Cui, X. Zhao, Q. Zhang, L. Gu, L. Zheng, L.H. Li, Q. Wu, D. J. Singh, D. Matsumura, T. Tsuji, Y.-T. Cui, J. Zhao, W. Zheng, Coordination Number Regulation of Molybdenum Single-Atom Nanozyme Peroxidase-like Specificity, *Chem* 7 (2021) 436–449.
- [35] X. Hu, G. Luo, Q. Zhao, D. Wu, T. Yang, J. Wen, R. Wang, C. Xu, N. Hu, Ru Single-Atoms on N-Doped Carbon by Spatial Confinement and Ionic Substitution Strategies for High-Performance Li-O₂ Batteries, *J. Am. Chem. Soc.* 142 (2020) 16776–16786.
- [36] W. Ye, S. Chen, Y. Lin, L. Yang, S. Chen, X. Zheng, Z. Qi, C. Wang, R. Long, M. Chen, J. Zhu, P. Gao, L. Song, J. Jiang, Y. Xiong, Precisely Tuning the Number of Fe Atoms in Clusters on N-Doped Carbon toward Acidic Oxygen Reduction Reaction, *Chem* 5 (2019) 2865–2878.
- [37] S. Ji, Y. Chen, Q. Fu, Y. Chen, J. Dong, W. Chen, Z. Li, Y. Wang, L. Gu, W. He, C. Chen, Q. Peng, Y. Huang, X. Duan, D. Wang, C. Draxl, Y. Li, Confined Pyrolysis within Metal–Organic Frameworks To Form Uniform Ru₃ Clusters for Efficient Oxidation of Alcohols, *J. Am. Chem. Soc.* 139 (2017) 9795–9798.
- [38] H. Shang, T. Wang, J. Pei, Z. Jiang, D. Zhou, Y. Wang, H. Li, J. Dong, Z. Zhuang, W. Chen, D. Wang, J. Zhang, Y. Li, Design of a Single-Atom Indium^{δ⁺}-N₄ Interface for Efficient Electroreduction of CO₂ to Formate, *Angew. Chem. Int. Ed.* 59 (2020) 22465.
- [39] M. Zhu, C. Zhao, X. Liu, X. Wang, F. Zhou, J. Wang, Y. Hu, Y. Zhao, T. Yao, L.-M. Yang, Y. Wu, Single Atomic Cerium Sites with a High Coordination Number for Efficient Oxygen Reduction in Proton-Exchange Membrane Fuel Cells, *ACS Catal.* 11 (2021) 3923–3929.
- [40] H. Zhou, T. Yang, Z. Kou, L. Shen, Y. Zhao, Z. Wang, X. Wang, Z. Yang, J. Du, J. Xu, M. Chen, L. Tian, W. Guo, Q. Wang, H. Lv, W. Chen, X. Hong, J. Luo, D. He, Y. Wu, Negative Pressure Pyrolysis Induced Highly Accessible Single Sites Dispersed on 3D Graphene Frameworks for Enhanced Oxygen Reduction, *Angew. Chem. Int. Ed.* 59 (2020) 20465.
- [41] W. Ni, Z. Liu, Y. Zhang, C. Ma, H. Deng, S. Zhang, S. Wang, Electroreduction of Carbon Dioxide Driven by the Intrinsic Defects in the Carbon Plane of a Single Fe-N₄ Site, *Adv. Mater.* 33 (2021) 2003238.
- [42] Y. Gao, Z. Chen, Y. Zhao, W. Yu, X. Jiang, M. He, Z. Li, T. Ma, Z. Wu, L. Wang, Facile synthesis of MoP-Ru₂P on porous N_x P co-doped carbon for efficiently electrocatalytic hydrogen evolution reaction in full pH range, *Appl. Catal. B-Environ.* 303 (2022), 120879.
- [43] Y. Gao, D. Zheng, Q. Li, W. Xiao, T. Ma, Y. Fu, Z. Wu, L. Wang, 3D Co₃O₄-RuO₂ Hollow Spheres with Abundant Interfaces as Advanced Trifunctional Electrocatalyst for Water-Splitting and Flexible Zn-Air Battery, *Adv. Funct. Mater.* 32 (2022) 2203206.
- [44] D. Wang, H. Xu, P. Yang, L. Xiao, L. Du, X. Lu, R. Li, J. Zhang, M. An, A dual-template strategy to engineer hierarchically porous Fe-N-C electrocatalysts for the high performance cathodes of Zn-air batteries, *J. Mater. Chem. A* 9 (2021) 9761–9770.
- [45] H. Xu, D. Wang, P. Yang, L. Du, X. Lu, R. Li, L. Liu, J. Zhang, M. An, A hierarchically porous Fe-N-C synthesized by dual melt-salt-mediated template as advanced electrocatalyst for efficient oxygen reduction in zinc-air battery, *Appl. Catal. B-Environ.* 305 (2022), 121040.
- [46] M. Wang, K. Sun, W. Mi, C. Feng, Z. Guan, Y. Liu, Y. Pan, Interfacial Water Activation by Single-Atom Co-N₃ Sites Coupled with Encapsulated Co Nanocrystals for Accelerating Electrocatalytic Hydrogen Evolution, *ACS Catal.* 12 (2022) 10771–10780.
- [47] W. Zhou, H. Su, Y. Li, M. Liu, H. Zhang, X. Zhang, X. Sun, Y. Xu, Q. Liu, S. Wei, Identification of the Evolving Dynamics of Coordination-Uncoligated Iron Atomic Active Sites under Reaction Conditions, *ACS Energy Lett.* 6 (2021) 3359–3366.
- [48] L. Peng, J. Yang, Y. Yang, F. Qian, Q. Wang, D.S. Waterhouse, L. Shang, T. Zhang, G.I.N. Waterhouse, Mesopore-Rich Fe-N-C Catalyst with FeN₄-O-NC Single-Atom Sites Delivers Remarkable Oxygen Reduction Reaction Performance in Alkaline Media, *Adv. Mater.* 34 (2022) 2202544.
- [49] Z. Jin, P. Li, Y. Meng, Z. Fang, D. Xiao, G. Yu, Understanding the inter-site distance effect in single-atom catalysts for oxygen electroreduction, *Nat. Catal.* 4 (2021) 615–622.